

# Three-dimensional EBSD study on the relationship between triple junctions and columnar grains in electrodeposited Co–Ni films

A. BASTOS, S. ZAEFFERER & D. RAABE

Max-Planck-Institut für Eisenforschung, Max-Planck-Str. 1, D-40237, Düsseldorf, Germany

**Key words.** 3D EBSD, electrodeposition, growth mechanisms, grain boundary character

## Summary

Electrodeposited nanocrystalline materials are expected to have a homogeneous grain size and a narrow grain size distribution. In Co–Ni electrodeposited films, however, under certain conditions an undesired columnar grain structure is formed. Fully automated three-dimensional (3D) orientation microscopy, consisting of a combination of precise material removal by focussed ion beam and subsequent electron backscatter diffraction (EBSD) analysis, was applied to fully characterize the grain boundaries of these columnar grains in order to gain further understanding on their formation mechanisms. Two-dimensional orientation microscopy on these films indicated that the development of columnar grains could be related to the formation of low-energy triple junctions. 3D EBSD allowed us to verify this suggestion and to determine the boundary planes of these triples. The triplets are formed by grain boundaries of different quality, a coherent twin on the  $\{10\bar{1}1\}$  plane, an incoherent twin and a large-angle grain boundary. These three boundaries are related to each other by a rotation about the  $\langle 11\bar{2}0 \rangle$  direction. A second particularity of the columnar grains is the occurrence of characteristic orientation gradients created by regular defects in the grain. Transmission electron microscopy was applied to investigate the character of the defects. For this purpose, a sample was prepared with the focussed ion beam from the last slice of the 3D EBSD investigation. From the TEM and 3D EBSD observations, a growth mechanism of the columnar grains is proposed.

## Introduction

Three-dimensional (3D) analysis methods are of great interest in material research. The description of microstructure characteristics as real grain size, grain shape and distribution in a sample volume are examples of interesting information that can be accomplished by 3D analysis techniques. Studies on the nature of grain boundaries can be well performed

by serial sectioning and subsequent orientation microscopy. Conventional ways for serial sectioning are the mechanical (Kral *et al.*, 1999; Lewis *et al.*, 2006; Rowenhorst *et al.*, 2006), chemical or electrochemical removal of layers of material, followed by orientation microscopy on each surface layer. This has, however, the disadvantage of low resolution in depth, relatively imprecise depth removal and difficulties in precise localization and positioning of the subsequent layers.

The use of the focussed ion beam (FIB) technique for serial sectioning allows highly controlled removal of thin layers of materials with a minimum slice thickness of approximately 50 nm. The combination of electron backscatter diffraction (EBSD)-based orientation microscopy with serial sectioning via FIB in a dual beam scanning electron microscope (SEM) allows a microstructure characterization of a sample with spatial resolution of about  $50 \times 50 \times 50 \text{ nm}^3$  (Zaefferer *et al.*, 2008).

The 3D EBSD–FIB method for microstructure characterization has made considerable progress over the past few years. Several examples of materials investigation with this technique can be found in the literature (Grober *et al.*, 2006; Konrad *et al.*, 2006; Uchic *et al.*, 2006; Zaafarani *et al.*, 2006; Ferry *et al.*, 2007; Rollet *et al.*, 2007).

In this paper, we report on a 3D orientation microscopy study of Co–20 at.% Ni prepared through a process of aqueous electrodeposition using a pulsed current. Our previous two-dimensional (2D) EBSD characterization (Bastos *et al.*, 2006) of electrodeposited Co–Ni films suggested that the development of columnar grains in deposits with low additive concentration is related to the formation of low-energy triple junctions. The aim of this work is, therefore, to study this relationship, to determine the grain boundary planes of the triple junctions by high-resolution 3D EBSD, thus to achieve further understanding of the microstructure evolution during film growth.

## Experimental

The investigated sample was prepared through a process of aqueous electrodeposition using a pulsed current as

Correspondence to: S. Zaefferer. Tel: 49 211 6792 803; Fax: 49 211 6792 333; e-mail: s.zaefferer@mpie.de

described in detail by Wu *et al.* (2005) and Wu (2004). The sample was deposited onto a mirror-finished surface of pure titanium plane. The electrodeposition bath contained 30 gL<sup>-1</sup> NiSO<sub>4</sub>·6H<sub>2</sub>O, 30 gL<sup>-1</sup> CoSO<sub>4</sub>·7H<sub>2</sub>O, 15 gL<sup>-1</sup> NiCl<sub>2</sub>·6H<sub>2</sub>O, 15 gL<sup>-1</sup> H<sub>3</sub>BO<sub>3</sub>, 10 gL<sup>-1</sup> NaCl and 0.02 g/L saccharin. The sample was produced at 35°C deposition temperature at a current density of 5.1 A dm<sup>-2</sup>. The bath was stirred during the entire deposition process. After the deposition, the sample was removed from the titanium substrate. The film had a final thickness of 90 µm and an average composition of Co–20 at.% Ni.

The samples were investigated by 2D and 3D orientation microscopy. The 2D investigations were carried out on the cross section and on the two surfaces of the film, one being in contact with the bath and the other with the substrate. The 2D measurements were carried out on a JEOL 6500 F field emission gun SEM equipped with an EDAX/TSL EBSD system working at 15 kV acceleration voltage. The set-up for the 3D investigations is described later.

#### *General set-up of the FIB–SEM experiment for 3D EBSD–based orientation*

The automated 3D EBSD study was conducted using a joint high-resolution field emission SEM–EBSD set-up together with a FIB system in a Zeiss XB1540 (Carl Zeiss SMT AG, Oberkochen, Germany) crossbeam instrument. For EBSD measurements, the EDAX/TSL OIMDC software and a Digiview camera were used; the microscope was operated at 15 kV acceleration voltage and the sample was positioned at a working distance of 14 mm. The 3D EBSD analysis involves highly precise and fully automated serial sectioning with the FIB, followed by orientation microscopy on each of those layers using high-resolution EBSD measurements. For the serial sectioning by ion-beam milling, the FIB was operated at 30 kV acceleration voltage. Details of the technique can be found in Zaeferrer *et al.* (2008). The spatial resolution of the 3D pixels depends on the required magnification and sample volume. The spatial resolution of the current system is prospectively to reach about 50 × 50 × 50 nm<sup>3</sup>.

#### *Set-up of the 3D EBSD experiment*

The optimum set-up for an analysis of the complete cross section with a reasonable number of slices was to select a cross-section plane for milling and orientation microscopy. To test the influence of the ion beam on the microstructure, a region of 8 µm width was milled from the Co–Ni deposit surface with a beam current of 500 pA for approximately 10 min. Subsequently, an EBSD map was measured on an area of 15 × 15 µm, which included this milled region. The microstructures of both areas were compared and the only difference observed was that the image quality of the region prepared with the ion beam was significantly better than that of the mechanical polished one.

Before starting the 3D EBSD analysis, the sample was mechanically grinded and polished, so that a sharp rectangular corner of two cross sections was prepared as shown in Fig. 1. The sample was then mounted on a cross-section sample holder in such a way that the corner was freely accessible. The holder was placed on a high pre-tilted stage (70° tilt) and inserted into the microscope.

Preliminary to the automated 3D EBSD measurement, the sample and the instrument were adjusted to run the automated process properly. For the analysis of the electrodeposited Co–Ni sample, first the sample was aligned in EBSD position (0° stage tilt, 70° sample tilt) so that the growth direction was perfectly lined up from left to right on the microscope screen. Subsequently, the stage was tilted to the milling position at 34°. At this tilt angle, the SEM and FIB beam cross-over point was determined and the milling position was saved. For finding precisely the same position at every new cycle a position marker is required. To this end, a cross was milled close to the measurement area into the sample surface. At every cycle, this marker was detected by software and the sample placed into its reference position by applying a shift of the FIB beam. To mill a volume of 90 µm × 20 µm × 100 nm (width × height × depth) per cycle a milling current of 500 pA was applied for 30 min. To avoid shadowing from the remaining sample as the milling depth increases, a second milling field was defined applying a milling current of 2 nA for 5 min. This coarse milling procedure was always performed before the fine milling, so that re-deposition of milled material on the analysis surface could be avoided. After every cycle, the milling field was moved 100 nm towards the sample; this means a slice of 100 nm was removed from the sample surface per cycle.

After the milling process was completely adjusted, the sample was tilted back to the EBSD position (stage tilt of 0°, sample tilt of 70°). With the CCD camera inserted into the microscope chamber, this position was saved and a reference image was taken, so that by cross correlation and beam shift, the cross-marker on the surface could be correctly positioned before every orientation map. The EBSD system was set up for a measurement on an area of 100 × 20 µm at a high measurement rate of 65–70 patterns per second. This could only be accomplished by minimizing pattern indexing calculation time. To this end, only one phase (the fcc phase) was used for on-line pattern indexing. The complete indexing was then performed off-line from the recorded Hough-peak data using the full crystallographic information. In this way, the on-line pattern indexing required only 60 min. Since the investigated volume was large and a high-resolution measurement was required, the measurement time was kept short to avoid any possible long-term instability of the instrument, in particular of the FIB gun.

After all parameters had been adjusted, the automated process was started. The number of slices, the milling depth and the images that should be saved for documentation of the process were defined beforehand. The number of slices was set

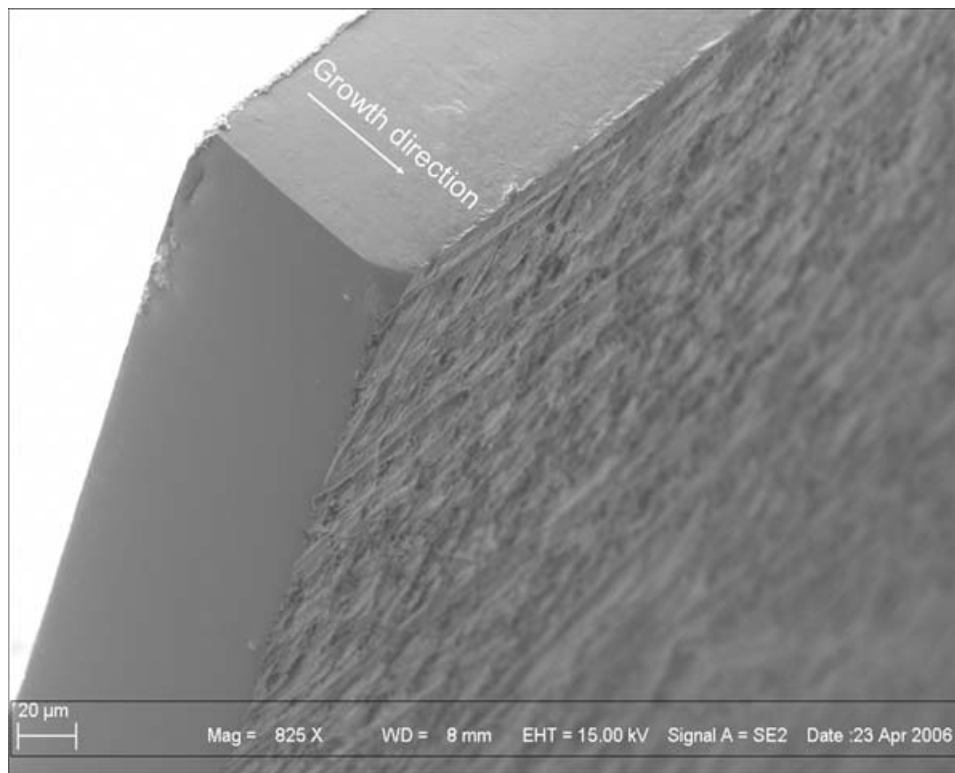


**Fig. 1.** Secondary electron image of the cross section of the Co–Ni thin film. The rectangular edge has been prepared by mechanical grinding and polishing. The front side surface corresponds to the deposit–bath interface, the back side to the deposit–substrate interface.

to 61 and the milling depth per step to 100 nm. A secondary electron (SE) image was saved after every milling process and before every EBSD map.

#### *TEM sample preparation from the last slice of the 3D EBSD investigation*

To observe the finest details of the cross-section microstructure, a sample was prepared for transmission electron microscope (TEM) from the last slice of the 3D EBSD volume using the FIB device.

To this end, the sample was positioned to milling position ( $34^\circ$ ). Figure 2 shows a schematic representation of the procedure for the cross-section TEM sample preparation by FIB. First an area of approximately  $10\ \mu\text{m}$  behind the prospected TEM-lamella (in Surface  $S_b$ ) was milled, so that only a thin layer of approximately  $2\ \mu\text{m}$  remained (Fig. 2 (b)). Subsequently, the sample was positioned such that the surface, where the TEM-lamella was still connected to the bulk sample, was perpendicular to the ion beam (Fig. 2 (c)). At this position, the tip of a Kleindieck nano-manipulator was attached to the TEM-lamella by deposition of a tungsten film between sample and manipulator (Fig. 2 (d)). Once the lamella was fixed, the remaining connection of the TEM-lamella to the bulk was cut (Fig. 2(e)), leaving the lamella only attached to manipulator

(Figs 2 (f) and 3(a) and (b)). At this point, the microscope chamber was opened and a half circle TEM sample grid was introduced into the microscope. The TEM-lamella was then attached to this grid (Fig. 2(g)) by another tungsten deposit. Finally, the manipulator tip was milled off from the sample (Fig. 3(c)). The still thick TEM sample was subsequently ion milled from both sides, until a thin foil of approximately 100 nm was obtained. The thinning of the sample was repeated at four different places along the cross section as it is shown in Fig. 3(d). The latter was necessary to maintain the stability of the thin sample, while being able to analyze a large area of the  $100\ \mu\text{m}$  long cross section. To avoid bending of the lamella, a region underneath the thin area was kept at a thickness of approximately  $2\ \mu\text{m}$ .

TEM investigations were carried out on an FEI CM20 TEM (FEI Company, Hillsboro, Oregon) at 200 kV. For measurement of crystal orientations and phases, the program Toca (Zaefferer, 2000) was used.

#### *3D visualization of the EBSD data*

For the 3D rendering procedure of the experimental data, we used the software 3DView developed by Zaefferer (Zaefferer *et al.*, 2008) and the non-commercial software package IMOD (Kremer *et al.* (1996)). Before 3D rendering, all data were first processed with the TSL-OIM software using a batch processing,

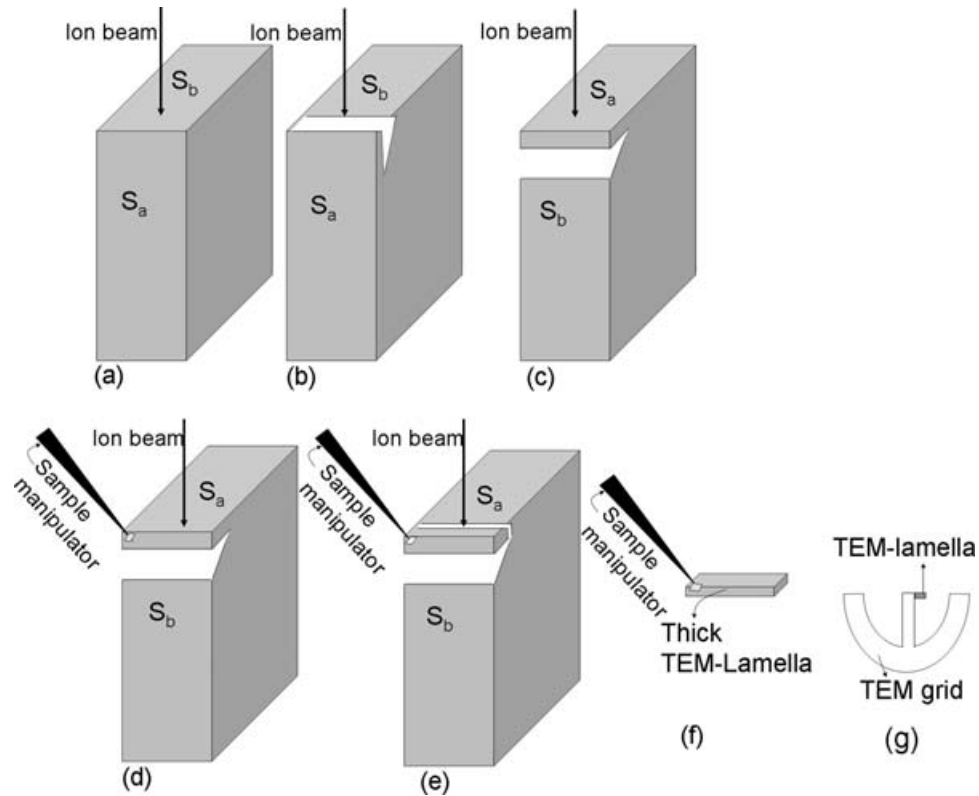


Fig. 2. Schematic representation of the preparation of a cross-section sample for TEM using a dual-beam microscope.

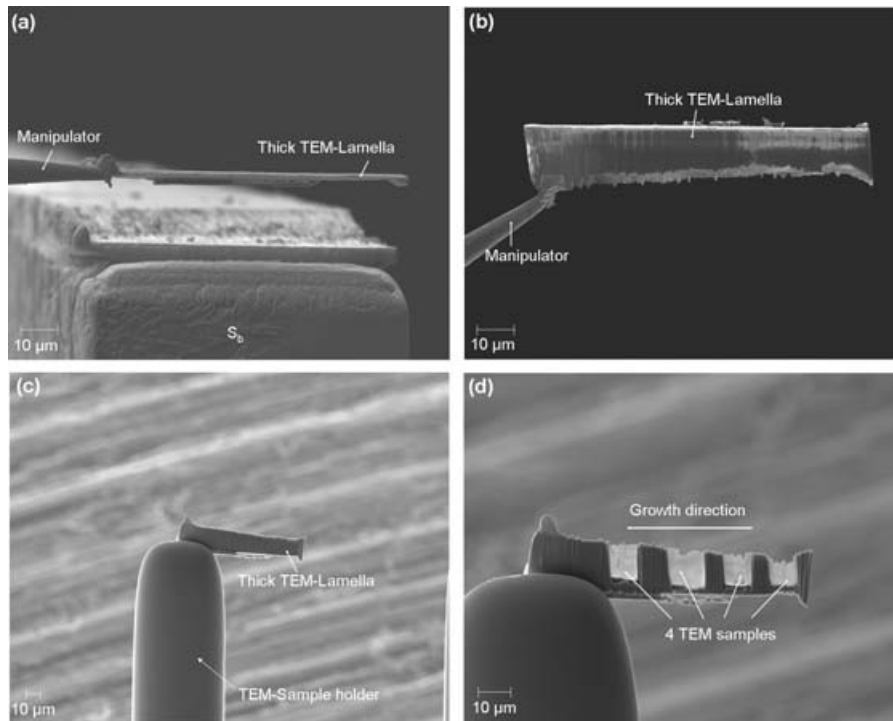


Fig. 3. TEM sample preparation using FIB. (a) TEM lamella removed from the bulk sample. (b) Thick TEM lamella attached to the sample manipulator; (c) Lamella attached to the half circle TEM sample grid; (d) Four TEM samples positioned across the full cross section with an approximate thickness of 100 nm attached to the TEM sample grid.

which allows the same set of analysis functions to be applied to several data sets. All 2D orientation maps were first cleaned up using algorithms provided by the OIM software that work on the confidence index (CI) for every measurement: first a 'CI standardization' assigned to every pixel within recognized grains the highest CI value found in that grain without changing the orientation of any pixel. Next, the 'CI neighbour correlation' algorithm assigned to pixels with a CI value lower than a predefined minimum of 0.05 the orientation of the pixel with the highest CI value in its direct neighbourhood. This clean-up procedure changed only 4% of the measured data points, most of them in areas close to grain boundaries. For the work presented here, a grain (in 2D) was defined as a region consisting of at least four connected points with misorientations of less than  $5^\circ$ . Subsequently, for each section, maps were created and saved showing the crystal orientation in inverse pole figure colouring, the phase, grain boundaries and the pattern quality.

The 3D rendering software is based on the stacking of the 2D EBSD maps and allows the visualization of any position in space of the measured volume. In addition, areas can be zoomed in and grain boundaries can be manually selected, which enables the determination of local grain boundary normals with respect to the sample and crystal reference systems.

the representation of three selected grains from the sample volume, the IMOD software was used. For this purpose, the requested individual grains had to be selected manually in every slice. Subsequently, a map consisting of only these three grains and their grain boundaries was saved for every slice. The IMOD software was then used to define the contours of the respective grains. IMOD uses a triangulation approach to construct an enveloping surface using the nodal points from each section. The three generated surfaces were then coloured arbitrarily and displayed using standard 3D rendering techniques.

## Results

### 2D EBSD characterization

A topographic analysis of the locations of the twin boundaries in the deposit-substrate and bath interface shows that in many cases two  $\langle\bar{2}110\rangle$   $57^\circ$  twins occur together with one  $63^\circ$ – $69^\circ$  boundary in a triple point with a common  $\langle 11\bar{2}0\rangle$  rotation axis. Figure 4(a) shows a pattern quality map of the deposit-bath interface where the arrangement of these triple junctions are highlighted by white triangles. The free grown surface of the electrodeposited film shows pyramidal clusters of three grains

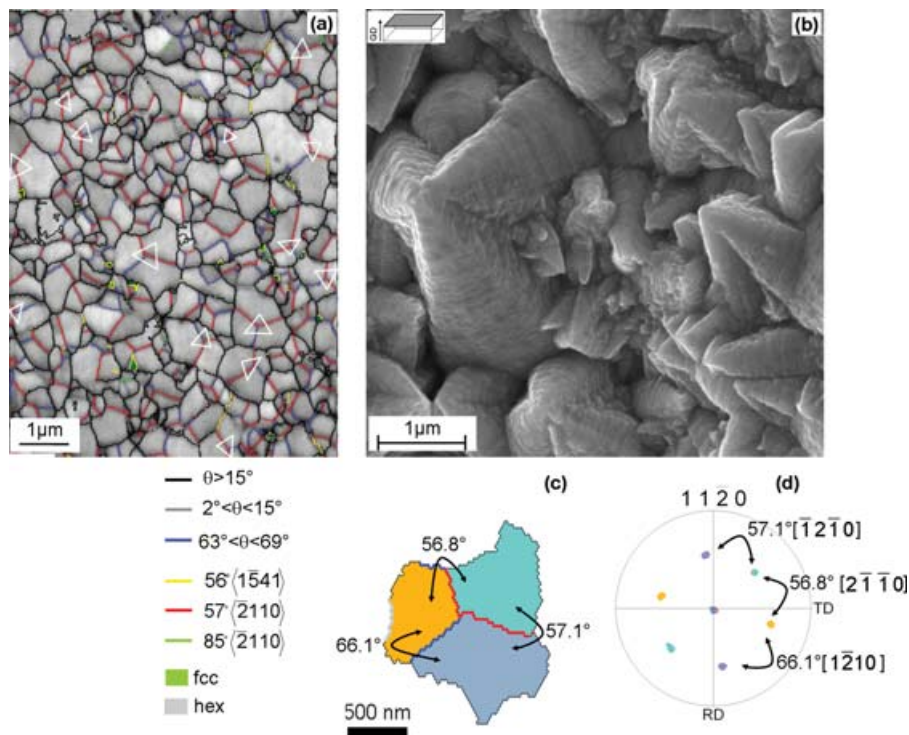


**Fig. 4.** (a) Pattern quality map of the deposit-bath interface showing the triple junctions (highlighted with white triangles) formed by two twin boundaries of  $\langle\bar{2}110\rangle$   $57^\circ$  (red) and a third boundary of  $63^\circ$ – $69^\circ$  misorientation (blue). Note that the microstructure contains a small amount of grains with fcc crystal structure and typical hcp-fcc phase boundaries (in yellow). (b) SEM micrograph of the deposit-bath interface showing the surface morphology of the deposit with threefold pyramids each consisting of three grains. (c) Three highlighted grains showing a triple junction arrangement and its corresponding pole figure (d).

**Table 1.** Fraction of triple points formed by two boundaries of misorientation between  $53^\circ$  and  $61^\circ$  and one boundary of misorientation between  $60^\circ$  and  $69^\circ$  and the density of these triple points as number per square micrometre of the deposit-substrate and bath interface.

	Deposit interface	
	Substrate	Bath
Fraction of triple points ( $57^\circ/57^\circ/66^\circ$ ) (%)	$7.9 \pm 3.1$	$6.6 \pm 3.5$
Density of triple points ( $57^\circ/57^\circ/66^\circ$ ) (Number $\mu\text{m}^{-2}$ )	$0.9 \pm 0.3$	$0.7 \pm 0.5$

growing together (Fig. 4 (b)). By careful FIB milling of the tips of these pyramidal clusters to a flat surface and performing an EBSD map on this area, it was shown that the three pyramidal grains are related to each other by exactly the same boundary configuration as the one described earlier, two twins of  $57^\circ$  misorientation and an arbitrary high-angle grain boundary of  $66^\circ$ . In Fig. 4 (c), one example of such a triple junction is shown, where the grains are arbitrarily coloured. Figure 4 (d) shows the  $\{11\bar{2}0\}$  pole figure plot of these three grains, which reveals the almost perfect rotation of this three grains about the common  $\langle 11\bar{2}0 \rangle$  axis, which is, in fact, the preferential growth direction of these grains.

The fraction of the special triple junctions was estimated for the deposit-substrate and bath interface. To this end, all triple points in the measured orientation maps were first exported into a list. All triple points containing two grain boundaries with a misorientation varying from  $53^\circ$  to  $61^\circ$  and a grain boundary with a misorientation varying from  $60^\circ$  to  $69^\circ$  were counted and the fraction was calculated. The rotation axes of these grain boundaries were not considered. Table 1 gives the average fraction and density of these triple points (number of triple points per square micrometre) determined from a sample area of  $3300 \mu\text{m}^2$  and of  $2000 \mu\text{m}^2$  for the deposit-substrate and bath interface, respectively.

The small variation of the fractions and densities of triples is related to the fact that with increasing deposit thickness,

the grain size (the grain diameter perpendicular to the growth direction) increases. The fraction of these triples is lower than 10% of the total amount of triple junctions. However, on every square micrometre, almost one set of these three grains is found on the substrate interface.

Figure 5 shows a pattern quality and grain boundary map of the cross section. It can be observed that the columnar grains are separated by either a twin boundary of  $57^\circ$  (red lines) or by an arbitrary large-angle grain boundary of a misorientation of approximately  $66^\circ$  (blue lines). The particular configuration of these triple junctions and the fact that they are found all over the sample indicates that these triples display a low-energy grain boundary arrangement. A further indication on the low energy of these boundaries will be given by the 3D investigations described in the next sections.

### 3D characterization

For understanding the relationship between the triplets of grain boundaries described earlier and the formation of columnar grains, we employed 3D EBSD-based orientation microscopy. Figure 6 shows the 3D inverse pole figure maps of the studied sample volume. In Fig. 6 (a), the growth direction is the reference direction for colouring, boundaries with misorientation  $\theta$  between  $2^\circ$  and  $15^\circ$  are shown in grey and those with  $\theta > 15^\circ$  in black. In Fig. 6 (b), the reference direction is a direction in the deposit plane; general large-angle grain boundaries are coloured black and possible twin boundaries white. The microstructure of the studied electrodeposited Co–Ni film is very complex, consisting of two grain classes, columnar and non-columnar ones. The columnar grains extend in growth direction to an average length of approximately  $10 \mu\text{m}$  and have an average diameter perpendicular to their growth direction of  $400 \text{ nm}$ . The non-columnar grains reveal a more equiaxed morphology with an average length in growth direction of  $700 \text{ nm}$  and perpendicular to it of  $200 \text{ nm}$ . A detailed study on the microstructure, texture and grain boundary characteristics of this film has been published elsewhere (Bastos *et al.*, 2006).

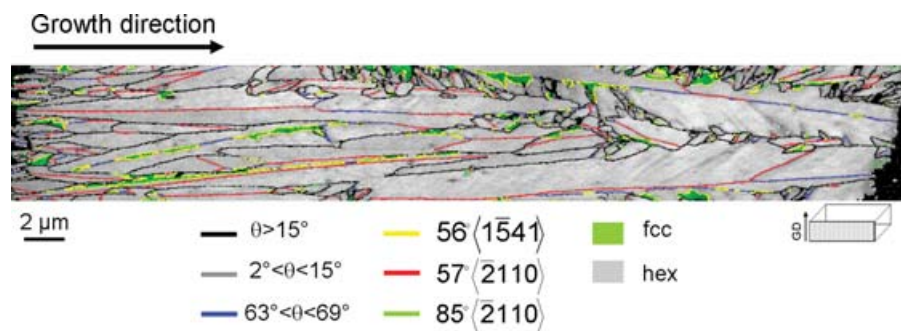


**Fig. 5.** EBSD pattern quality map of the sample cross section displaying the phases (fcc: green; hexagonal: grey), and the boundary character between the phases and twin boundaries.

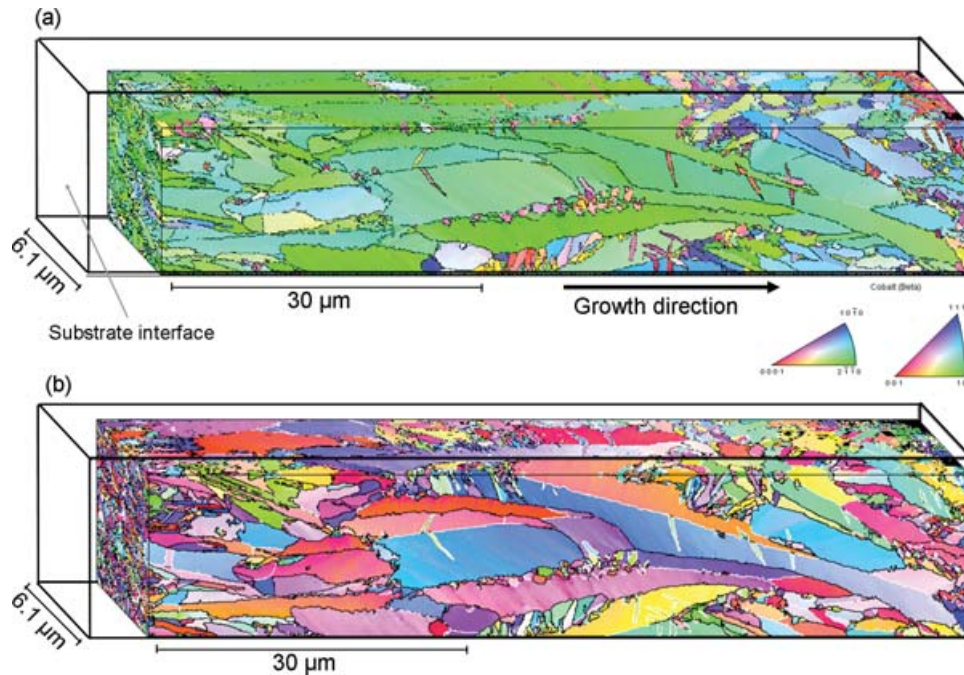


**Fig. 6.** Three-dimensional inverse pole figure map of the electrodeposited Co–Ni. (a) Colouring reference direction is the growth direction, black lines represent large-angle and grey low-angle grain boundaries. (b) Reference direction is a direction in the deposit plane, white boundaries represent possible twin boundaries, black large-angle and grey low-angle grain boundaries (analyzed volume of  $85\ \mu\text{m} \times 20\ \mu\text{m} \times 6.1\ \mu\text{m}$ ).

A typical twin triple that was completely included in the analyzed volume was chosen for the characterization of the grain boundary planes. Figure 7 (a) shows the 3D microstructure and a cut (A) parallel to the growth direction along a plane that contains the studied triple. In this 3D view grain, (2) is not visible as it is on the top of grain (1). Figure 7 (b) shows the 3D model representation of cut (A) as reconstructed with IMOD, where only grain (1) and (3) can be observed. Figure 7 (c) reveals the representation of all three studied grains reconstructed with the IMOD software. At a film thickness of  $5\ \mu\text{m}$  (position I in Fig. 7 (a)), two twin-related grains enter the measured volume. These two grains have a sharp  $57^\circ \langle 11\bar{2}0 \rangle$  twin relation already when grain (1) is first observed in the measured volume. Only after further  $5\ \mu\text{m}$  growth, the grain (3) occurs and grows parallel to grain (1) and (2) as a very fine cylinder (position II in Figs 7 (a) and (b)). After further  $10\ \mu\text{m}$  of growth, grain (3) expands perpendicular to growth direction. At this position, all three grains have the  $\langle 11\bar{2}0 \rangle$  crystallographic direction parallel to the macroscopic film growth direction. This position was selected for determination of the grain boundary characteristics (position III in Figs 7 (a) and (b)). Figure 8 shows another representation of the studied grains by showing three cuts perpendicular to the growth direction. Here position II and III are illustrated again, and the triple is highlighted inside the sample volume (cut a, b and c).

Figure 9 (from Zaefferer *et al.*, 2008) shows a schematic representation of this triple with its grain boundaries where

the growth direction is perpendicular to the image plane. The figure indicates that the grain boundary plane between grain (1) and (2) is a coherent twin boundary on the  $\{10\bar{1}1\}$  plane. Grain (3), although it shows the correct twin orientation relation to grain (2), does not have a coherent twin boundary with the latter. This is indicated by the fact that the planes on both sides of the grain boundary are very different, the one of grain (2) being very precisely the (0001) basal plane, the other one being some quite highly indexed one. The boundary between grain (1) and (3) does not show any typical twin relationship; however, the plane of grain (1) is also precisely the (0001) basal plane.

As it could be observed in Figs 7 (a) and (b), the triple does not grow in a straight line through the film, but is strongly curved. This is related to the occurrence of strong in-grain misorientations that were already reported in an earlier study by 2D orientation microscopy (Bastos *et al.*, 2006). In this study, we showed that the shorter a grain is, the higher is its orientation gradient (misorientation per micrometre). Figure 10 shows the orientation deviation of the grains along the growth direction in the 3D volume. The colours indicate orientation deviations to a maximum of  $20^\circ$  with respect to the average orientation of each individual grain. This orientation deviation is caused by the regular occurrence of lattice defects in the crystal, which turn the  $\langle 11\bar{2}0 \rangle$  crystal direction away from the macroscopic growth direction. TEM observations have shown that these defects are dislocations and stacking faults.

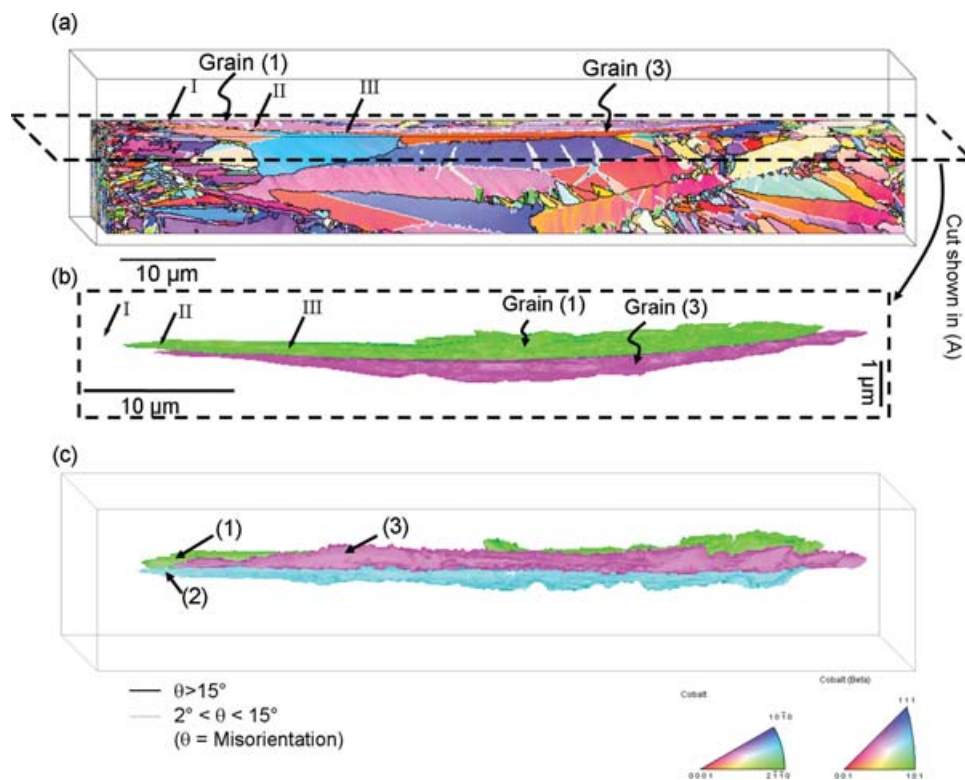


**Fig. 7.** (a) Three-dimensional inverse pole figure map of a direction perpendicular to film growth showing a cut along the plane marked in the image. Possible twin boundaries are shown in white, high-angle grain boundaries in black and low-angle grain boundaries in grey. In this representation, grain (2) is not visible as it is on top of grain (1). (b) Model showing the grain curvature at cut (A). (c) Representation of the three grains analyzed in the microstructure volume. Grains reconstructed with IMOD (b and c). The colours are chosen arbitrarily and serve only to separate the three grains.

### Comparison with TEM observations

As described before, a TEM lamella was prepared by FIB from the last slice of the 3D EBSD measurement. Figure 11 (a) shows the 2D EBSD map of slice 61, whereas Fig. 11 (b) shows the TEM micrograph of the highlighted area in (a). Because of the necessary thinning of the TEM lamella to a thickness of approximately 100 nm and because of the tilt angle of the TEM sample, differences in the microstructure of both images arise. The microstructure seen in the TEM is approximately 1  $\mu\text{m}$  deeper in the bulk sample as the EBSD map. The bright-field image Fig. 11 (b) shows a section of three columnar grains (A–C). Grain (C) is illustrated again in Fig. 11 (c). The bright and dark contrast observed in this grain is equivalent to the misorientation along the growth direction observed by 2D and 3D EBSD and indicates a periodic rotation of the crystal. A trace analysis on an interface between bright and dark contrast reveals a common  $(11\bar{2}0)$  plane and a rotation on the  $\langle 10\bar{1}0 \rangle$  axes. Following the orientation gradient throughout the grain (from point 1 to 13 in Fig. 11 (e)), a continuous rotation of the crystal can be observed (Fig. 11 (f)). Because of the complexity of this lattice rotation and because of the high defect density of the sample, it is difficult to extract from this analysis a possible reason for the crystal rotation.

It can only be speculated that the rotation is caused by sets of dislocations that are continually built into the crystal lattice by incoherent nucleation of new atom layers (Korzlov & Bicelli, 2000; Merchant, 1995). Figure 11 (d) shows a non-columnar grain with a high density of regular defects. The trace analysis of these ordered interfaces reveals a common (0001) plane, which indicates either stacking faults on the (0001) basal plane or phase boundaries between very thin lamellae of fcc and hcp cobalt phase. However, here the TEM image interpretation is difficult – probably also because of the high strain contrast caused by the FIB sample preparation. A direct comparison between both grains shown in Figs 11 (c) and (d) reveals that the non-columnar grain (d) has a significantly higher density of defects than the columnar grain (c).

### Discussion

The high density of special triple junctions and the large volume fraction of columnar grains indicate the importance of these features for the growth of the electrodeposited film. In a first approach, we suggested the following mechanism of triple junction formation based on conventional 2D EBSD: A primary crystal twins independently with the same twin relationship ( $57^\circ \langle 11\bar{2}0 \rangle$ ) into two twin variants such that all

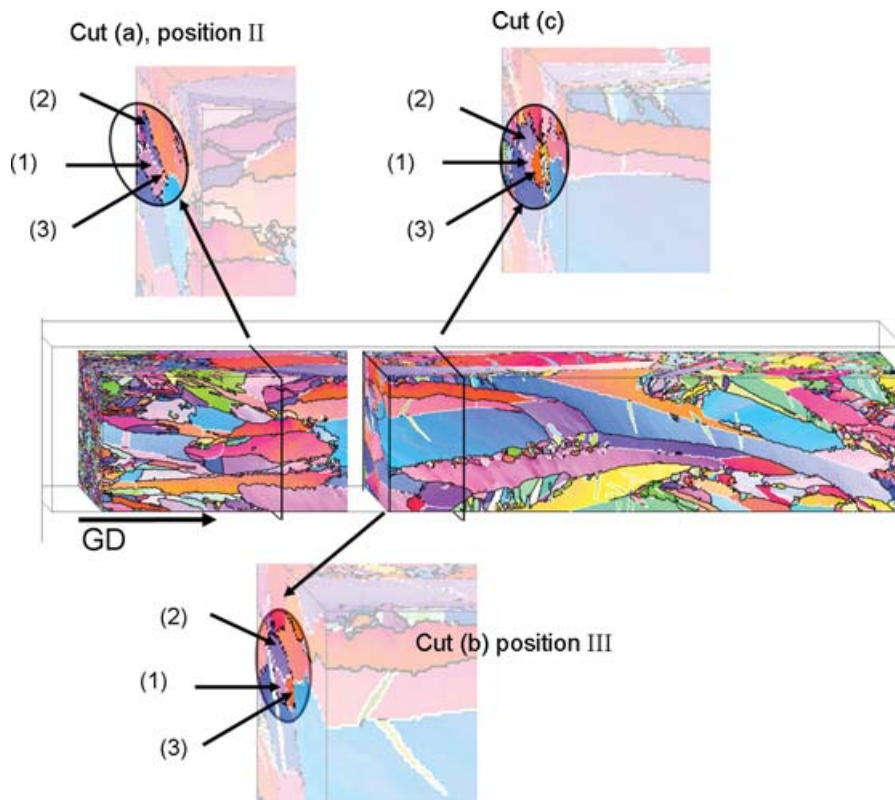


Fig. 8. Cuts (perpendicular to the growth direction) through the three-dimensional microstructure showing the arrangement of the three analyzed grains in growth direction. Cut (a) shows position II, where grain (3) nucleates and starts growing as a fine cylinder. Cut (b) shows the position III. At this position (20  $\mu\text{m}$  from the substrate), the grain boundary planes were analyzed (see Fig. 9). Cut (c) shows three grains at a film thickness of 30  $\mu\text{m}$ .

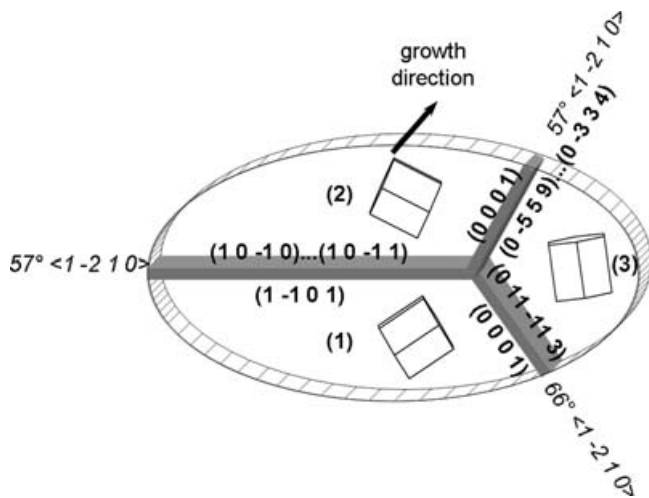


Fig. 9. Schematic three-dimensional representation of the twin triples and their boundaries frequently observed in the deposits. Grain (1) and (2) form a coherent  $57^\circ \langle 11\bar{2}0 \rangle$  twin. Grain (3) is in a non-coherent twin relation to grain (2), but it has no special relationship with (1). Note the occurrence of basal planes as boundary planes between (2) and (3) and (1) and (3).

three crystals show a common  $\langle 11\bar{2}0 \rangle$  direction parallel to the film growth direction. The third boundary would then be automatically fixed to a  $66^\circ \langle 11\bar{2}0 \rangle$  relationship (Bastos *et al.*, 2006). The results of the 3D analysis showed that this proposal is not entirely correct. The triple is formed by boundaries of quite different quality, a coherent and an incoherent twin and a conventional large-angle grain boundary, all of them are related to each other by a rotation about the  $\langle 11\bar{2}0 \rangle$  direction. The grain boundary of the incoherent twin and the arbitrary boundary both show a (0001) boundary plane in one of the abutting crystals. It seems that the coherent twin plane as well as the (0001) basal planes form low-energy grain interfaces.

It is interesting to observe that the low-energy triples are strongly curved. This curvature is caused by the regular incorporation of lattice defects that rotate the three crystal lattices and by the fixed orientation relation between the three grains. As explained later, the incorporation of lattice defects is due to the activity of additive molecules on the growing surface. It is, however, not clear, why this leads to such regular defect arrangements as those observed here.

During the electrodeposition process, the existence of low-energy grain boundaries should promote the crystal growth at these sites because more energy is required to form new atom layers in sites of higher energy. Also, the nucleation of new

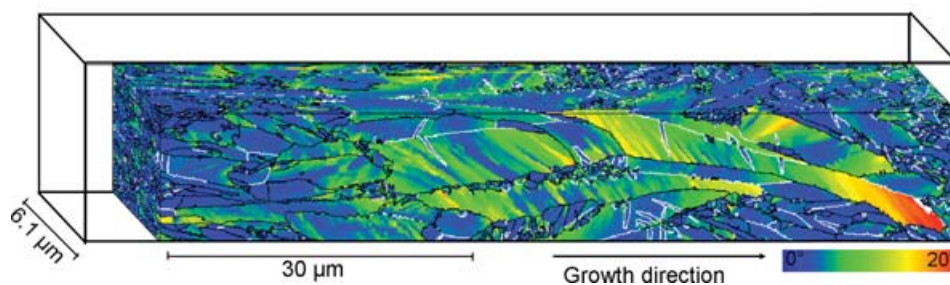


Fig. 10. Three-dimensional orientation gradient map for a maximum gradient of  $20^\circ$  from the grain average orientation. Possible twin boundaries are shown in white, high-angle grain boundaries in black and low-angle grain boundaries in grey. See next side for caption.

grains requires more energy; consequently, the probability for continued growth of columnar grains increases.

The length of the columnar grains is not only related to the formation of low-energy triple junctions but also to the defect density in the crystal lattice, which is related to the over-potential occurring during the electrodeposition process, the pH of the deposition solution and the additive concentration (Merchant, 1995; Gabe, 1997). The free growing surface of electrodeposited Co–Ni from baths with low additive concentration reveals a considerably higher fraction of triple grain pyramids than the fraction of long columnar grains. In addition, the length of the columnar triples scatters significantly. It occurs therefore that most of the crystals grow in the form of triples and, depending on the defect density, these triples are long or short.

The formation of columnar grains on electrodeposited Co–Ni samples is, therefore, related to two competitive processes. On the one hand, low-energy grain boundaries facilitate the addition of atoms at these sites thus promoting localized growth. On the other hand, during electrocrystallization, defects are built into the crystal lattice by co-deposition of hydrogen and other impurities (Vértes *et al.*, 1984; Kumar, 2003). These defects rotate the crystal away from the quick growing  $\langle 11\bar{2}0 \rangle$  direction. This continuous deviation slowly hinders further crystal growth. At high defect densities, the crystal is deflected faster from the preferential crystal growth direction and further growth becomes difficult. Grains with high defect density are therefore over-grown by grains with low defect density. According to the literature, the defect density being built into the lattice is affected by the local concentration of additives that can be incorporated into the crystal lattice (Merchant, 1995; Korzlov & Bicelli, 1998, 2000). Because of the quick growth of certain crystals, a pronounced surface roughness is created that possibly causes local changes in electrolytic conditions and solution concentration and leads to locally different growth conditions. It may be assumed that this triggers the formation of the observed clusters of non-columnar grains in between the long columnar grains. The presence of additive molecules on growth sites interferes on the nucleation by blocking the ion reduction at these sites thus stimulating growth in other sites and by forcing semi-

coherent nucleation on top of the adsorbed molecule causing defects in the crystal (Reddy, 1963; Amblard *et al.*, 1979). When the additive concentration is high, ions arriving at the deposit interface find fewer sites for coherent incorporation and incoherent growth becomes more pronounced. In this way, new grains with large-angle grain boundaries are formed.

It is interesting to observe that the low-energy triple grains are conserved along the full length of the columnar grains although they are strongly curved. The curvature is caused by the regular incorporation of lattice defects that rotate all three grains in a similar way. Because of the fixed orientation relation between the three grains, the triple junction thus bends accordingly. It is not clear why the incorporation of lattice defects is as regular as we observe it here, but it is related to the activity of additive molecules on the surface.

## Conclusions

Fully automated 3D orientation microscopy was applied to study a relatively large volume of an electrodeposited Co–Ni film with high resolution ( $100 \text{ nm}^3$  in all three dimensions). The analysis of the 3D microstructure allowed the determination of the grain boundary planes of the frequently observed triple junctions consisting of triples of three grains with two  $57^\circ \langle 11\bar{2}0 \rangle$  twin boundaries and a third arbitrary boundary with a misorientation of approximately  $66^\circ$ . The formation of a low-energy grain boundary configuration consisting of a coherent twin plane as well as the basal plane (0001) facilitates the development of a columnar grain morphology in Co–Ni deposits. Because of the co-deposition of impurities, defects are built in to the crystal lattice that cause the deflection of the crystal from the preferential growth direction. The higher is the defect density the faster is the deviation and the shorter is the grain.

A TEM investigation was performed on the last slice of the 3D EBSD measurement to study these defects. However, the high defect density in the sample and the high strain contrast probably caused by the FIB sample preparation made it difficult to determine their nature. It was, however, at least possible to identify the habit plane of the defects and the axes of crystal rotation caused by them. Further investigations are necessary

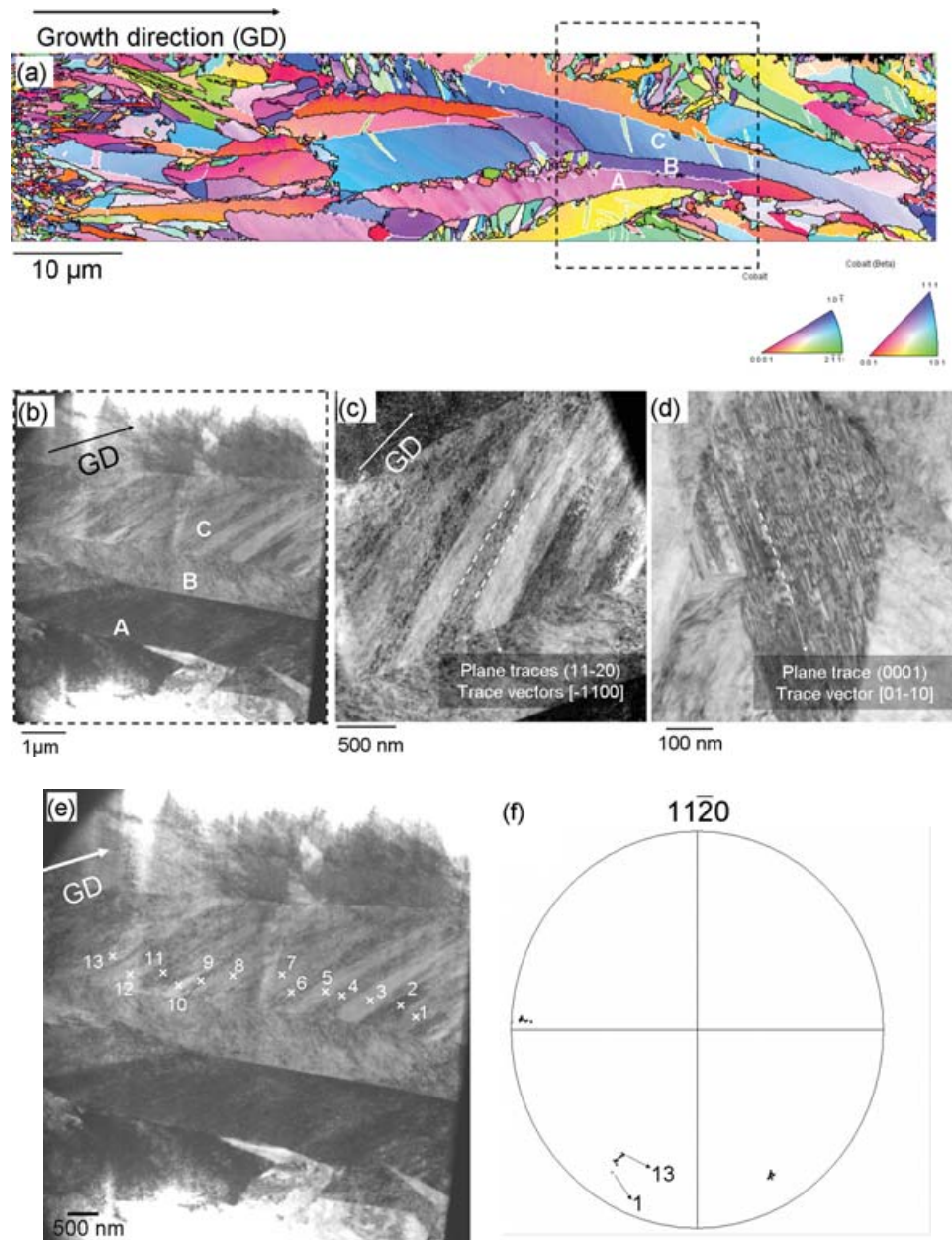


**Fig. 11.** (a) Inverse pole figure map of the last slice of the 3D EBSD study, colouring according to a reference a direction perpendicular to the film growth direction. (b) TEM micrograph of the highlighted area in (a). (c) Analysis of the boundary traces in columnar grain (C). (d) Stacking fault trace analysis in a non-columnar grain. (e) Columnar grain C and points where orientation analyses were performed. (f)  $\{11\bar{2}0\}$  pole figure plot showing the continuous rotation of grain C. Orientation measurements of point 1–13.

to completely understand the origin of the crystal rotation and its relation to the film deposition conditions.

## References

- Amblard, J., Epelboin, I., Froment, M. & Maurin, G. (1979) Inhibition and nickel electrocrystallization. *J. Appl. Electrochem.* **9**, 233–242.
- Bastos, A., Zaeferrer, S., Raabe, D. & Schuh, C. (2006) Characterization of the microstructure and texture of nanostructured electrodeposited NiCo using electron backscatter diffraction (EBSD). *Acta Mater.* **54**, 2451–2462.
- Ferry, M., Xu, W., Mateescu, N., Cairney, J.M. & Humphreys, F.J. (2007) On the viability of FIB tomography for generating 3D orientation maps in deformed and annealed metals. *Mater. Sci. Forum.* **550**, 55–64.
- Groeber, M.A., Haley, B.K., Uchic, M.D., Dimiduk, D.M. & Ghosh, S. (2006) 3D reconstruction and characterization of polycrystalline microstructures using a FIB–SEM system. *Mater. Charact.* **57**, 259–273.

- Gabe, D.R. (1997) The role of hydrogen in metal electrodeposition processes. *J. Appl. Electrochem.* **27**, 908–915.
- Konrad, J., Zaefferer, S. & Raabe, D. (2006) Investigation of orientation gradients around a hard Laves particle in a warm-rolled Fe3Al-based alloy using a 3D EBSD-FIB technique. *Acta Mater.* **54**, 1369–1380.
- Kral, M.V. & Spanos, G. (1999) Three-dimensional analysis of proeutectoid cementite precipitates. *Acta Mater.* **47**, 711–724.
- Kremer, R., Mastrorade, D.N. & McIntosh, J.R. (1996) Computer visualization of three-dimensional image data using IMOD. *J. Struct. Biol.* **116**, 71–76.
- Kozlov, V.M. & Bicelli, L.P. (2000) Influence of noncoherent nucleation on the formation of polycrystalline structure of metals electrodeposited in the presence of surface active agents. *Mater. Chem. Phys.* **62**, 158–163.
- Kozlov, V.M., Bicelli, L.P. & Timoshenko, V.N. (1998) Influence of foreign particle adsorption on the formation of structural defects during noncoherent nucleation: an atomistic analysis. *J. Cryst. Growth* **183**, 456–462.
- Kumar, K.S., Van Swygenhoven, H. & Suresh, S. (2003) Mechanical behavior of nanocrystalline metals and alloys. *Acta Mater.* **51**, 5743–5774.
- Lewis, A.C., Bingert, J.F., Rowenhorst, D.J., Gupta, A., Geltmacher, A.B. & Spanos, G. (2006) Two- and three-dimensional microstructural characterization of a super-austenitic stainless steel. *Mater. Sci. Eng. A* **418**, 11–18.
- Merchant, H. (1995) *Defect Structure, Morphology and Properties of Deposits* (ed. by H. Merchant). The Minerals, Metals & Materials Society, Warrendale, PA.
- Reddy, A.K.N. (1963) Preferred orientations in nickel electro-deposits. *J. Electroanal. Chem.* **6**, 141–152.
- Rollet, A.D., Lee, S.-B., Campman, R. & Rohrer, G.S. (2007) Three-dimensional characterization of microstructure by electron back-scatter diffraction. *Annu. Rev. Mater. Res.* **37**, 627–658.
- Rowenhorst, D.J., Gupta, A., Feng, C.R. & Spanos, G. (2006) 3D crystallographic and morphological analysis of coarse martensite: combining EBSD and serial sectioning. *Scr. Mater.* **55**, 11–16.
- Uchic, M.D., Groeber, M.A., Dimiduk, D.M. & Simmons, J.P. (2006) 3D microstructural characterization of nickel superalloys via serial-sectioning using a dual beam FIB-SEM. *Scr. Mater.* **55**, 23–28.
- Vertes, A., Szeles, Cs., Kajcsos, Zs. & Leidheiser Jr. H. (1984) Structure studies of nickel electrodeposits. *J. Electrochem. Soc.* **131**, 1526–1531.
- Wu, B.Y.C. (2004) *MS Thesis in Materials Science and Engineering*. Massachusetts Institute of Technology, Cambridge.
- Wu, B.Y.C., Ferreira, P.J. & Schuh, C.A. (2005) Nanostructured Ni-Co alloys with tailorable grain size and twin density. *Metall. Mater. Trans.* **36A**, 1927–1936.
- Zaafarani, N., Raabe, D., Singh, R.N., Roters, F. & Zaefferer, S. (2006) Three-dimensional investigation of the texture and microstructure below a nanoindent in a Cu single crystal using 3D EBSD and crystal plasticity finite element simulations. *Acta Mater.* **54**, 1863–1876.
- Zaefferer, S. (2000), New developments of computer-aided crystallographic analysis in transmission electron microscopy. *J. Appl. Crystallogr.* **33**, 10–25.
- Zaefferer, S., Wright, S.I. & Raabe, D. (2008), 3D orientation microscopy – a new dimension of microstructure characterisation. *Metall. Mater. Trans.* **39A**, 374–389.